

## Coexistence of Active and Hydrodynamic Turbulence in Two-Dimensional Active Nematics

C. Rorai,<sup>1</sup> F. Toschi<sup>2,3</sup> and I. Pagonabarraga<sup>1,4,5</sup>

<sup>1</sup>*CECAM, Centre Européen de Calcul Atomique et Moléculaire, École Polytechnique Fédérale de Lausanne (EPFL), Batochime, Avenue Forel 2, 1015 Lausanne, Switzerland*

<sup>2</sup>*Department of Applied Physics, Eindhoven University of Technology, Den Dolech 2, 5600 MB Eindhoven, Netherlands*

<sup>3</sup>*CNR-IAC, I-00185 Rome, Italy*

<sup>4</sup>*Departament de Física de la Matèria Condensada, Universitat de Barcelona, C. Martí i Franquès 1, 08028 Barcelona, Spain*

<sup>5</sup>*University of Barcelona Institute of Complex Systems (UBICS), Universitat de Barcelona, 08028 Barcelona, Spain*

 (Received 16 May 2022; revised 29 September 2022; accepted 25 October 2022; published 18 November 2022)

In active nematic liquid crystals, activity is able to drive chaotic spatiotemporal flows referred to as active turbulence. Active turbulence has been characterized through theoretical and experimental work as a low Reynolds number phenomenon. We show that, in two dimensions, the active forcing alone is able to trigger hydrodynamic turbulence leading to the coexistence of active and inertial turbulence. This type of flow develops for sufficiently active and extensile flow-aligning nematics. We observe that the combined effect of an extensile nematic and large values of the flow-aligning parameter leads to a broadening of the elastic energy spectrum that promotes a growth of kinetic energy able to trigger an inverse energy cascade.

DOI: [10.1103/PhysRevLett.129.218001](https://doi.org/10.1103/PhysRevLett.129.218001)

Active fluids, such as microbial suspensions, cytoskeletal suspensions, self-propelled colloids, and cell tissues, are complex fluids distinguished by the presence of an active phase whose single units self-propel [1–3]. The collective dynamics of the self-driven elements can generate spontaneous flows characterized by chaotic spatiotemporal patterns, referred to as active or mesoscale turbulence [1,4–6]. Active turbulence is subject to intense investigation using a wide variety of theoretical models [1] ranging from phenomenological generalizations of the Navier-Stokes (GNS) equations [5] to equations for active liquid crystals [7] with either nematic or polar order. Understanding active turbulence is relevant in biological and ecological systems to describe nutrient mixing and molecular transport at the microscale [8–10]. Identifying the universal features of active turbulence and its similarities with hydrodynamic turbulence where the motion is dominated by the nonlinear terms of the Navier-Stokes equations, namely, the inertial terms, remains an open challenge [1].

Experimentally, active turbulence is a low Reynolds number,  $Re$ , phenomenon [6,11]. Theoretically, it has been described emerging from an ensemble of vortices whose area is exponentially distributed and whose isotropic kinetic energy spectrum in two dimensions follows a  $k^{-1}$  or  $k^{-4}$  power law, depending on whether the wave number  $k$  is smaller or larger than a characteristic vortex size [12]. Initial comparisons with computer simulations provided convincing evidence of the  $k^{-4}$  scaling, while the  $k^{-1}$  power

law was later confirmed by high-resolution Stokes flow numerical simulations [13].

Active fluids have also attracted interest for their rheological behavior. Theoretical work showed that, in the regime of linear rheology, activity either thins or thickens the flow depending on the swimmers' propulsion mechanism (pushers vs pullers) and their response to shear (flow tumbling vs flow aligning) [14,15]. Notably, experiments [16] confirmed the theoretical prediction of an inviscid superfluidlike regime for pusher-type bacterial suspensions, for which active turbulence may be influenced by inertia, a circumstance of interest for 2D flows, where the inverse energy cascade can drive flows up to the system-size scale. This consideration opens up new scenarios that challenge active turbulence as a merely low- $Re$  number phenomenon.

Although a 2D modified version of the GNS equation [17] has shown that active turbulence can spontaneously trigger hydrodynamic turbulence [18], the active nemato-hydrodynamic (AN) model [7,19], derived from conservation laws and system symmetries, has parameters with a direct physical meaning, allowing for an insightful understanding of the mechanisms causing turbulence.

In this work we report the coexistence of active and hydrodynamic turbulence in 2D active nematics. The coupled active-hydrodynamic turbulent state is linked to a distribution of elastic energy across scales that emerges as the combined effect of an extensile nematics and large flow-aligning parameters. This feature is intrinsic to active nematics, even in low- $Re$  number flows; however, it is at

TABLE I. Simulation parameters in a system of size  $L$ . The grid and time spacing are taken as reference units.  $T_{\text{fin}}$  is the final simulation time,  $\text{Re}^*$  is the nominal Re number,  $\text{Re}^* = \sqrt{K\alpha q_0}L/(\nu^2\rho)$ , and  $l_a = \sqrt{K/|\alpha|}$  is the nominal active length, see SM. 118 simulations were run.

Group	$L$	$T_{\text{fin}}$	$\text{Re}^*$	$l_a$	$\xi$
A	560	$10^7$	0.055	-3.26, -2.45, -1/2, 1/2, 0.87, 1, 1.73, 2.45, 3.26	0, 1, 2
B	560	$5 \times 10^5$	5.5	0.5, 0.87, 1.0, 1.73, 2.45, 3.26	0, 1, 2
B	560	$5 \times 10^5$	5.5	-6.5, -6.0, -5.5	1
B	560	$5 \times 10^5$	5.5	-1/2, -1, -2.45, -3.26, -3.5, -3.75	2
B	560	$5 \times 10^5$	5.5	-1/5, -2.45, -3.26, -4.5, -5	0,1
C	560	$5 \times 10^5$	22	-3.26, -2.45, -1, -1/2, 1, 2.45, 3.26	0,1,2
C	560	$5 \times 10^5$	22	-1/5	0,1
C	560	$5 \times 10^5$	22	-0.4, -0.3, -1/4	2
C	560	$5 \times 10^5$	22	1/2	0
D	2240	$10^7$	0.22	0.87, 2.45	0
D	2240	$\geq 3 \times 10^7$	0.22	-1/2, 1/2	0, 1/2, 1, 3/2, 2
E	2240	$10^6$	22	1/2, 0.87, 1, 1.73, 2.45, 3.26	0
E	2240	$2 \times 10^6$	22	1/2, 2.45	1
E	2240	$2 \times 10^6$	22	1/2, 0.87, 1, 1.73, 2.45	2
F	6144	$1.03 \times 10^6$	60	-1/2, 1/2	2

intermediate Re numbers that it triggers the inverse energy cascade leading to large Re number flows.

The AN model [7,19,20] couples the evolution of the nematic phase with the incompressible Navier-Stokes equation endowed by a modified stress term. The nematic phase is represented by a second-order tensor:  $Q_{ij} = q_0(n_i n_j - \delta_{ij}/2)$ , where  $\delta_{ij}$  is the Kronecker delta,  $q_0$  is the magnitude of the orientational order, and  $n_i$  is the director field. The model adopts the Landau-de Gennes free energy  $\mathcal{F} = \int d^3r [(K/2)(\partial_k Q_{ij})^2 + (A/2)Q_{ij}Q_{ji} + (B/3)Q_{ij}Q_{jk}Q_{ki} + (C/4)(Q_{ij}Q_{ji})^2]$ , where  $K$  is the elastic constant. The relaxation of the orientational order is controlled by the molecular field tensor  $\mathcal{H}_{ij} = -(\delta\mathcal{F}/\delta Q_{ij}) + (\delta_{ij}/2)\text{Tr}(\delta\mathcal{F}/\delta Q_{kl})$ . The equations for the nematic order parameter,  $Q_{ij}$ , and the velocity field,  $u_i$ , read

$$(\partial_t + u_k \partial_k)Q_{ij} - S_{ij} = \Gamma \mathcal{H}_{ij}, \quad (1)$$

$$(\partial_t + u_k \partial_k)u_i = \frac{1}{\rho} \partial_j \Pi_{ij}, \quad (2)$$

complemented by incompressibility,  $\partial_k u_k = 0$ .  $\Gamma$  is the rotational diffusivity,  $S_{ij}$  the corotation term,  $\rho$  the fluid density, and  $\Pi_{ij}$  the pressure term. The corotation term is given by  $S_{ij} = (\xi E_{ik} + \Omega_{ik})(Q_{kj} + \delta_{kj}/2) + (Q_{ik} + \delta_{ik}/2) \times (\xi E_{kj} - \Omega_{kj}) - 2\xi(Q_{ij} + \delta_{ij}/2)(Q_{kl}\partial_k u_l)$ , where  $E_{ik}$  and  $\Omega_{ik}$  are the strain rate and vorticity tensor, respectively, while  $\xi$  is the flow-aligning parameter and controls whether the active material is flow aligning or flow tumbling. The pressure term is given by the sum of a hydrodynamical, passive nematic and active nematic contribution:  $\Pi_{ij} = \Pi_{ij}^{\text{hydro}} + \Pi_{ij}^{\text{passive}} + \Pi_{ij}^{\text{active}}$ , where  $\Pi_{ij}^{\text{hydro}} = -P\delta_{ij} + 2\eta E_{ij}$ ,

$\Pi_{ij}^{\text{passive}} = 2\xi(Q_{ij} + \delta_{ij}/2)(Q_{kl}\mathcal{H}_{lk}) - \xi\mathcal{H}_{ik}(Q_{kj} + \delta_{kj}/2) - \xi(Q_{ik} + \delta_{ik}/2)\mathcal{H}_{kj} - \partial_i Q_{kl}(\delta\mathcal{F}/\delta\partial_j Q_{lk}) + Q_{ik}\mathcal{H}_{kj} - \mathcal{H}_{ik}Q_{kj}$  and  $\Pi_{ij}^{\text{active}} = -\alpha Q_{ij}$ , with  $\alpha$  the activity parameter;  $\alpha \geq 0$  ( $\leq 0$ ) for a contractile (extensile) active nematic.

We integrate Eqs. (1) and (2) in a 2D periodic domain using a hybrid lattice-Boltzmann finite-difference method [20,21]. We impose a zero velocity field and a director field oriented along  $x$  and randomly perturbed by 10% white noise as initial conditions. We explore a wide portion of parameter space (Table I) and find that systems mostly evolve toward an active turbulent state, Fig. 1(a), or a state where active and hydrodynamic turbulence coexist, Figs. 1(b) and 1(c). In both cases the multiscale nature of the flow is revealed by the presence of structures of different sizes, however, the largest structures reach the system size only when inertial turbulence is triggered.

We classify as *active turbulent*, systems that reach a statistical steady state characterized by energy spectra with the scaling predicted in Refs. [12,13]. In these systems, the contribution of inertia is marginal, see the low Re numbers in Fig. 2(a). Figure 2(a) displays the kinetic energy spectra,  $E_{\text{kin}}(k)$ , for active turbulent flows: the predicted  $k^{-4}$  scaling is always visible unlike the  $k^{-1}$  large-scale scaling, observed only for sufficiently low Re numbers and high resolutions, see Supplemental Material (SM) [22] for further details on the scaling [23]. As opposed to the case in which  $\text{Re} = 0$  Ref. [13], the peak of the elastic energy spectrum does not coincide with the one of the kinetic energy spectrum: see in Fig. 2(a) the position of the effective active wave number  $k_a = 2\pi/\tilde{l}_a$ , corresponding to the first moment of the elastic energy spectrum,  $E_{\text{el}}(k)$ .

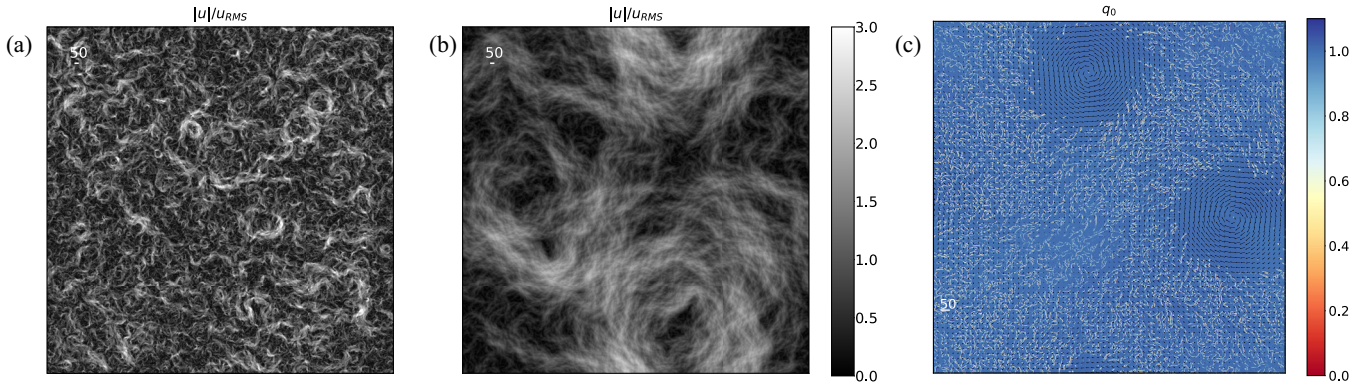


FIG. 1. Snapshots of the magnitude of the velocity field rescaled by the root-mean-square velocity over the entire system (same scale) for the contractile (a) and extensile (b) nematic of group  $F$  at time  $T_{\text{fin}}$ , see Table I. See the SM for visualizations of the vorticity and scalar order parameter. (c) Magnitude of the tensor order parameter (in color) and velocity field (black arrows) for the last time step of the run of group  $E$  with  $\alpha > 0$ ,  $l_a = 0.5$  and  $\xi = 2$ . Unlike contractile nematics (a), the velocity field for extensile nematics (b) and (c) generates large scale structures that span all the system size. See movies and SM. The white segment in the three panels is of 50 unit length.

Inertial and active turbulence coexist when the flows develop a condensate state composed by a system spanning vortex pair [25,26], Fig. 1(c). Condensation is a finite-size effect expected in forced 2D hydrodynamic turbulence when large scale drag is absent [27]. The convergence to the condensate state is signaled by (i) the formation of large scale structures, Figs. 1(b) and 1(c), (ii) the scaling of the total kinetic energy density,  $E_{\text{kin,tot}} = \int_0^\infty E_{\text{kin}}(k)dk$ , as  $t^1$  [25], see Fig. 2(b) inset, and (iii) a large-scale scaling of  $E_{\text{kin}}(k)$  consistent with  $k^{-5/3}$  and  $k^{-3}$  at the largest wave numbers where the finite size effects are felt [25], see Fig. 2(b). Because of the steady growth of the largest modes these systems have not reached a steady state. However, the small and intermediate scales have converged: compare in Fig. 2(b) the spectra averaged over the last time steps (in color) with the instantaneous spectra in the time window

where the average is performed (gray). The signature of active turbulence is recognizable at smaller scales where the kinetic energy scales as  $k^{-4}$ , Fig. 2(b).

We explore parameter space systematically, beyond Figs. 1 and 2, covering flow-tumbling  $\xi < 1$  and flow-aligning  $\xi > 1$  regimes for both  $\alpha < 0$  and  $\alpha > 0$  and different active lengths, system sizes, and Re numbers: see Table I. Active nematics reach three different states: an active turbulent (AT) state as in Figs. 1(a) and 2(a), coupled active and hydrodynamic turbulence (AHT state) as in Figs. 1(b) and 1(c), and 2(b), and a nonturbulent (NT) state. We classify as *nonturbulent*, systems that do not display a Gaussian velocity distribution and a well-developed isotropic kinetic energy spectrum. These correspond to slowly varying time-dependent flows whose topological features are walls that reconfigure in time [28,29], see SM.

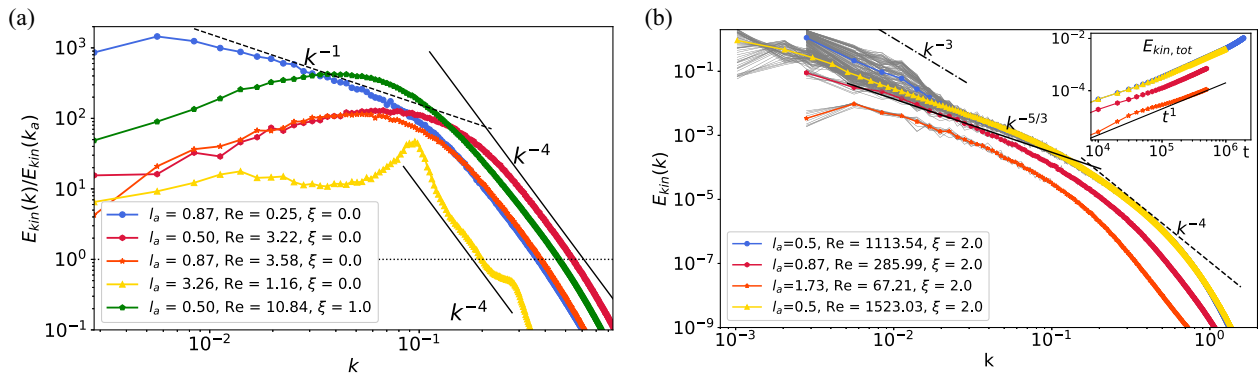


FIG. 2. (a) Isotropic kinetic energy spectra rescaled by the kinetic energy at the active wave number  $k_a$  identified by the intersection of the spectra with the dotted line. Black lines identify the  $k^{-4}$  (solid) and  $k^{-1}$  (dashed) scaling. The curves correspond to simulations of group  $E$  and  $D$  (Table I). (b) Kinetic energy spectra and total kinetic energy density vs time (inset) in simulation units for systems of groups  $E$  and  $F$  characterized by the coexistence of active and inertial turbulence. Note the large Re numbers and  $\xi$  and the different large scale scaling compared to the runs of panel (a) where inertial effects are negligible. See SM for the definitions of the isotropic kinetic,  $E_{\text{kin}}(k)$ , and elastic,  $E_{\text{el}}(k)$ , energy spectra.

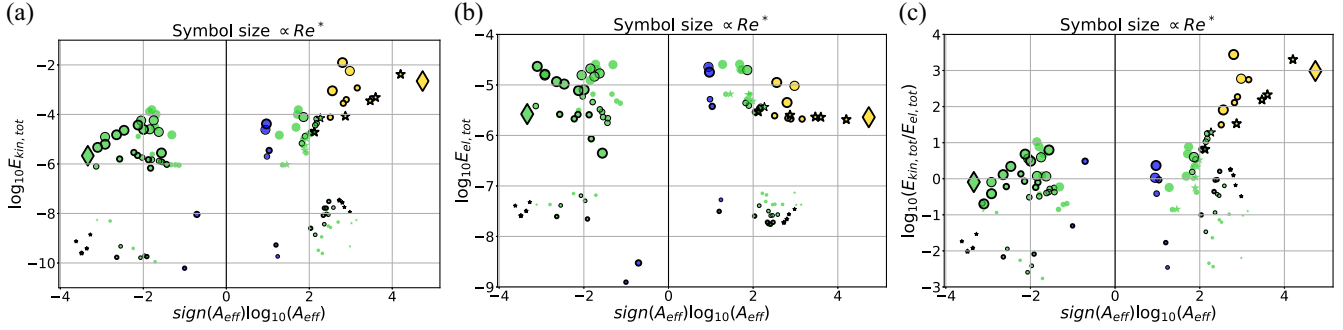


FIG. 3. Logarithm of the total kinetic (a) and elastic (b) energy vs  $A_{\text{eff}}$ , that compares the characteristic size of the largest flow structures  $\tilde{L}_I$  with the effective active length scale  $\tilde{l}_a$  at which energy is injected into the system, for the simulations of Table I. The different colors refer to the different types of steady states: nonturbulent (blue), active turbulent (green), coupled active and inertial turbulence (orange). The size of the marker is proportional to the nominal Re number,  $\text{Re}^*$ , while the different symbols correspond to different resolutions  $L = 560$  (circle),  $L = 2240$  (star),  $L = 6144$  (diamond). The linewidth of the black symbols edge is proportional to  $\xi$ :  $\xi = 0$  (no edge),  $\xi = 1$  (thin edge)  $\xi = 2$  (thick edge). (c) Ratio between the kinetic and elastic energy. Runs where active and hydrodynamic turbulence coexist are present only in the positive semiplane.

To identify boundaries in phase space between the NT and the AT states and between the AT and the AHT states, Fig. 3 displays the total kinetic energy density and the total elastic energy density,  $E_{\text{el,tot}} = \int_0^\infty E_{\text{el}}(k)dk$ , for all the runs of Table I as a function of an effective active parameter

$A_{\text{eff}} = 2q_0\tilde{L}_I^2/(\tilde{l}_a^2\Gamma\eta)$  where  $\tilde{L}_I$  is the first moment of the kinetic energy spectrum and represents the characteristic size of the largest flow structures, while  $\tilde{l}_a$  represents the scale at which energy is injected through active forcing; see SM for further considerations. In Fig. 3 the data are

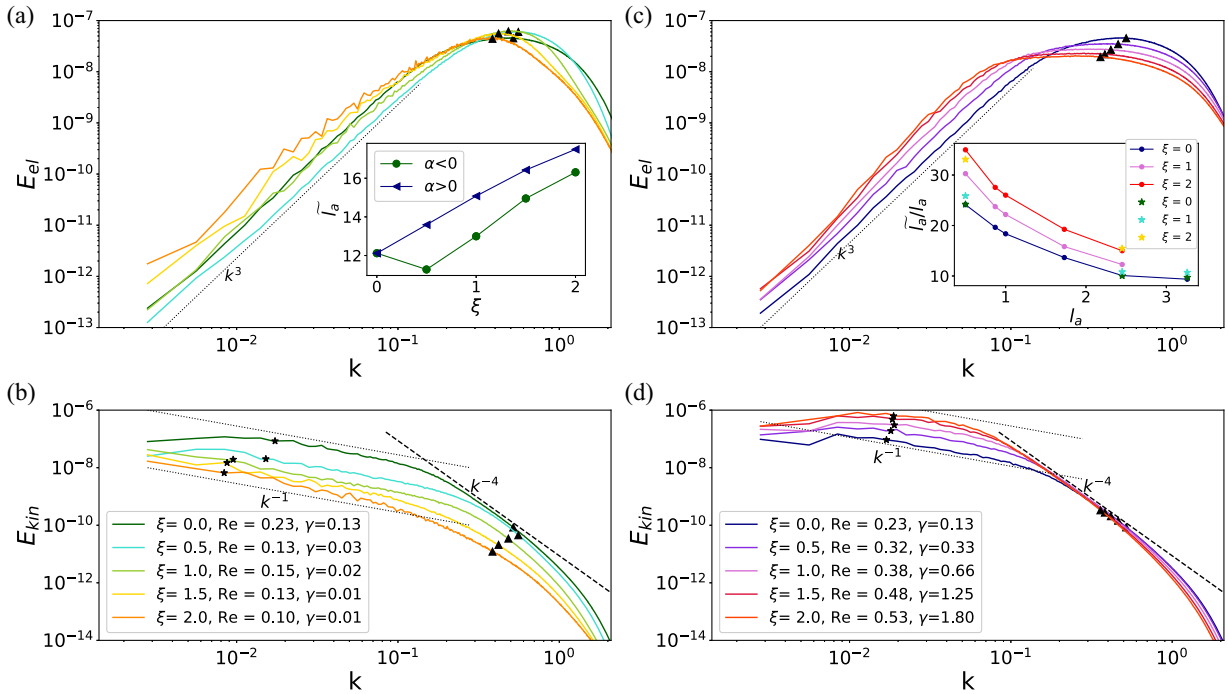


FIG. 4. Elastic (a),(c) and kinetic (b),(d) energy spectra in simulation units for simulations of group D with  $l_a = -0.5$  (a),(b) and  $l_a = 0.5$  (c),(d) and different values of the flow-aligning parameter  $\xi$  as reported in the legend of panel (b) and (d). The same color code is used in panels (a),(b) and (c),(d). The effective active wave number  $k_a = 2\pi/\tilde{l}_a$  is marked by black triangles while the wave number corresponding to the integral length scale,  $\tilde{L}_I$ , is marked by a star in panel (b) and (d). The inset of panel (a) shows how the effective active length,  $\tilde{l}_a$ , varies with  $\xi$  for contractile and extensile nematics whose spectra are shown in this image. The inset of panel (c) shows how  $\tilde{l}_a$  scaled by  $l_a$  varies with  $l_a$  for group A excluding those in a NT state. The increase of  $\xi$  affects the spectra of a contractile and extensile nematics differently.

distinguished by the state of the system (different colors), the value of  $Re^*$  (different symbol sizes), by the system size (different symbols), and by the flow-aligning parameter (different line-width); see SM for a visualization of the data grouped by  $\xi$ . The plot shows that the three dynamical states can be separated by equal  $A_{\text{eff}}$  lines. Figure 3 reveals striking asymmetries between the negative and positive semiplane: (i) no AHT runs are found in the negative semiplane, (ii) the transition from the NT to the AT state occurs for smaller  $A_{\text{eff}}$  for contractile nematics and for different types of flows, see SM, (iii) the largest kinetic energies are associated with the lowest  $\xi$  for a contractile nematic, the opposite is true for an extensile nematic and the runs that display an inverse energy cascade have  $\xi \geq 1$ , (iv)  $E_{\text{kin,tot}}$  increases with  $A_{\text{eff}}$ , except for the most energetic flows in the negative semiplane where it decreases with  $|A_{\text{eff}}|$ , (v)  $E_{\text{el,tot}}$ , despite showing a reduced variability compared to  $E_{\text{kin,tot}}$ , tends to decrease with  $|A_{\text{eff}}|$  except for a contractile nematics with  $\xi = 2$ . Figure 3(c) displays the ratio between the kinetic and elastic energy in logarithmic scale, showing that generically for contractile active flows the elastic energy dominates over the kinetic energy, while the opposite is true for extensile active flows.

The kinetic and elastic energy spectra for extensile and contractile nematics, Fig. 4, show that flows characterized by a positive and negative activity respond differently to an increase of the flow-aligning parameter. An increase of  $\xi$  results in an increase of the effective active length  $\tilde{l}_a$ , that is, an increase in the correlation length of the  $Q_{ij}$  tensor [30]. This is observed both for contractile and extensile nematics and reveals that the characteristic length of the nematic structures increases with  $\xi$  (insets of Fig. 4 and SM). However,  $E_{\text{el}}(k)$  shows that  $\xi$  affects the redistribution of energy across scales differently for a contractile and extensile nematics. An increase of  $\xi$  causes the peak of  $E_{\text{el}}(k)$  to sharpen for a contractile nematics, Fig. 4(a), while in an extensile nematics,  $E_{\text{el}}(k)$  flattens considerably indicating that the highly energetic structures span a wider range of scales, Fig. 4(c); this is reflected in a wider range of wave numbers where the kinetic energy scaling follows the  $k^{-4}$  power law. The broadening of the  $k^{-4}$  power law to larger scales results in an increase of the kinetic energy as also evidenced by an increase of the ratio  $\gamma$  between the kinetic and elastic energy [legend of Fig. 4(d)]. This mechanism, intrinsic to the coupled effect of an extensile nematics and a large  $\xi$ , can trigger inertial turbulence through the inverse kinetic energy cascade if the  $Re$  number of a reference  $\xi = 0$  flow is large enough.

To conclude, we have unveiled a mechanism to rationalize the coexistence of active and inertial turbulence for active extensile and flow-aligning nematics. Remarkably, our finding that large  $Re$  number flows develop for extensile and flow-aligning nematics mirrors the experimental results of superfluidlike behavior for elongated pusherlike bacteria [16]. However, drawing closer analogies is challenging due to the lack of data on the flow

characteristics, e.g., large scale coherent motion vs active turbulent flow, when a negligible viscosity is measured inside the rheometer.

We acknowledge funding from the European Union's Horizon 2020 research and innovation program under the Marie Skłodowska-Curie Grant Agreement No. 754462. I.P. acknowledges support from Ministerio de Ciencia, Innovación y Universidades (Grant No. PGC2018-098373-B-100/FEDER-EU), DURSI (Grant No. 2017 SGR 884), and SNSF (Project No. 200021-175719). This work was supported by a grant from the Swiss National Supercomputing Centre (CSCS) under project ID s1079.

- 
- [1] R. Alert, J. Casademunt, and J.-F. Joanny, Active turbulence, *Annu. Rev. Condens. Matter Phys.* **13**, 143 (2022).
  - [2] M. C. Marchetti, J.-F. Joanny, S. Ramaswamy, T. B. Liverpool, J. Prost, M. Rao, and R. A. Simha, Hydrodynamics of soft active matter, *Rev. Mod. Phys.* **85**, 1143 (2013).
  - [3] S. Ramaswamy, The mechanics and statistics of active matter, *Annu. Rev. Condens. Matter Phys.* **1**, 323 (2010).
  - [4] V. Bratanov, F. Jenko, and E. Frey, New class of turbulence in active fluids, *Proc. Natl. Acad. Sci. U.S.A.* **112**, 15048 (2015).
  - [5] J. Dunkel, S. Heidenreich, M. Bär, and R. E. Goldstein, Minimal continuum theories of structure formation in dense active fluids, *New J. Phys.* **15**, 045016 (2013).
  - [6] H. H. Wensink, J. Dunkel, S. Heidenreich, K. Drescher, R. E. Goldstein, H. Lowen, and J. M. Yeomans, Meso-scale turbulence in living fluids, *Proc. Natl. Acad. Sci. U.S.A.* **109**, 14308 (2012).
  - [7] S. P. Thampi and J. M. Yeomans, Active turbulence in active nematics, *Eur. Phys. J. Special Topics* **225**, 651 (2016).
  - [8] H. Kurtuldu, J. S. Guasto, K. A. Johnson, and J. P. Gollub, Enhancement of biomixing by swimming algal cells in two-dimensional films, *Proc. Natl. Acad. Sci. U.S.A.* **108**, 10391 (2011).
  - [9] S. Mukherjee, R. K. Singh, M. James, and S. S. Ray, Anomalous Diffusion and Levy Walks Distinguish Active from Inertial Turbulence, *Phys. Rev. Lett.* **127**, 118001 (2021).
  - [10] R. Ran, Q. Brosseau, B. C. Blackwell, B. Qin, R. L. Winter, and P. E. Arratia, Bacteria hinder large-scale transport and enhance small-scale mixing in time-periodic flows, *Proc. Natl. Acad. Sci. U.S.A.* **118**, 2108548118 (2021).
  - [11] C. Dombrowski, L. Cisneros, S. Chatkaew, R. E. Goldstein, and J. O. Kessler, Self-Concentration and Large-Scale Coherence in Bacterial Dynamics, *Phys. Rev. Lett.* **93**, 098103 (2004).
  - [12] L. Giomi, Geometry and Topology of Turbulence in Active Nematics, *Phys. Rev. X* **5**, 031003 (2015).
  - [13] R. Alert, J.-F. Joanny, and J. Casademunt, Universal scaling of active nematic turbulence, *Nat. Phys.* **16**, 682 (2020).

- [14] Y. Hatwalne, S. Ramaswamy, M. Rao, and R. A. Simha, Rheology of Active-Particle Suspension, *Phys. Rev. Lett.* **92**, 118101 (2004).
- [15] L. Giomi, T. B. Liverpool, and M. C. Marchetti, Sheared active fluids: Thickening, thinning, and vanishing viscosity, *Phys. Rev. E* **81**, 051908 (2010).
- [16] H. M. López, J. Gachelin, C. Douarche, H. Auradou, and E. Clément, Turning Bacteria Suspensions into Superfluids, *Phys. Rev. Lett.* **115**, 028301 (2015).
- [17] J. Słomka and J. Dunkel, Generalized Navier-Stokes equations for active suspensions, *Eur. Phys. J. Special Topics* **224**, 1349 (2015).
- [18] M. Linkmann, G. Boffetta, M. C. Marchetti, and B. Eckhardt, Phase Transition to Large Scale Coherent Structures in Two-Dimensional Active Matter Turbulence, *Phys. Rev. Lett.* **122**, 214503 (2019).
- [19] P.-G. de Gennes and J. Prost, *The Physics of Liquid Crystals* (Oxford University Press, New York, 1993).
- [20] C. Rorai, F. Toschi, and I. Pagonabarraga, Active nematic flows confined in a two-dimensional channel with hybrid alignment at the walls: A unified picture, *Phys. Rev. Fluids* **6**, 113302 (2021).
- [21] D. Vincenzi, P. Perlekar, L. Biferale, and F. Toschi, Impact of the Peterlin approximation on polymer dynamics in turbulent flows, *Phys. Rev. E* **92**, 053004 (2015).
- [22] See Supplemental Material at <http://link.aps.org/supplemental/10.1103/PhysRevLett.129.218001> for further details on how spectral quantities and relevant parameters are computed, a description of the formation of large scale structures, comments on the density of defects and the  $k^{-4}$  scaling, details on the characteristics of the observed non-turbulent flows, and extra plots of the kinetic and elastic energy density as a function of the effective active parameter.
- [23] Previous studies [24] that included the inertial term in Eq. (2) also found  $E_{\text{kin}}(k)$  to differ from the  $k^{-1}$  power law at large scales.
- [24] J. Urzay, A. Doostmohammadi, and J. M. Yeomans, Multi-scale statistics of turbulence motorized by active matter, *J. Fluid Mech.* **822**, 762 (2017).
- [25] M. Chertkov, C. Connaughton, I. Kolokolov, and V. Lebedev, Dynamics of Energy Condensation in Two-Dimensional Turbulence, *Phys. Rev. Lett.* **99**, 084501 (2007).
- [26] J. Laurie, G. Boffetta, G. Falkovich, I. Kolokolov, and V. Lebedev, Universal Profile of the Vortex Condensate in Two-Dimensional Turbulence, *Phys. Rev. Lett.* **113**, 254503 (2014).
- [27] A. Alexakis and L. Biferale, Cascades and transitions in turbulent flows, *Phys. Rep.* **767–769**, 1 (2018).
- [28] L. Giomi, L. Mahadevan, B. Chakraborty, and M. F. Hagan, Excitable Patterns in Active Nematics, *Phys. Rev. Lett.* **106**, 218101 (2011).
- [29] L. Giomi, M. J. Bowick, P. Mishra, R. Sknepnek, and M. C. Marchetti, Defect dynamics in active nematics, *Phil. Trans. R. Soc. A* **372**, 20130365 (2014).
- [30] S. P. Thampi, R. Golestanian, and J. M. Yeomans, Driven active and passive nematics, *Mol. Phys.* **113**, 2656 (2015).